



LAWRENCE  
LIVERMORE  
NATIONAL  
LABORATORY

# Simulation of Spheromak Evolution and Energy Confinement

B.I. Cohen, E.B. Hooper, R.H. Cohen, D.N. Hill, H.S.  
McLean, R.D. Wood, S. Woodruff, C.R. Sovinec, G.A.  
Cone

November 10, 2004

46th Annual Meeting of the Division of Plasma Physics  
Savannah, GA, United States  
November 13, 2004 through November 19, 2004

## **Disclaimer**

---

This document was prepared as an account of work sponsored by an agency of the United States Government. Neither the United States Government nor the University of California nor any of their employees, makes any warranty, express or implied, or assumes any legal liability or responsibility for the accuracy, completeness, or usefulness of any information, apparatus, product, or process disclosed, or represents that its use would not infringe privately owned rights. Reference herein to any specific commercial product, process, or service by trade name, trademark, manufacturer, or otherwise, does not necessarily constitute or imply its endorsement, recommendation, or favoring by the United States Government or the University of California. The views and opinions of authors expressed herein do not necessarily state or reflect those of the United States Government or the University of California, and shall not be used for advertising or product endorsement purposes.

## **Simulation of Spheromak Evolution and Energy Confinement**

B.I. Cohen, E.B. Hooper, R.H. Cohen, D.N. Hill,

H.S. McLean, R.D. Wood, and S. Woodruff

University of California Lawrence Livermore National Laboratory

Livermore, CA 94550

C.R. Sovinec and G.A. Cone

Department of Engineering Physics

University of Wisconsin-Madison, Madison, WI 53706-1609

Simulation results are presented that illustrate the formation and decay of a spheromak plasma driven by a coaxial electrostatic plasma gun, and that model the energy confinement of the plasma. The physics of magnetic reconnection during spheromak formation is also illuminated. The simulations are performed with the three-dimensional, time-dependent, resistive magnetohydrodynamic NIMROD code. The simulation results are compared to data from the SSPX spheromak experiment at the Lawrence Livermore National Laboratory. The simulation results are tracking the experiment with increasing fidelity (e.g., improved agreement with measurements of the magnetic field, fluctuation amplitudes, and electron temperature) as the simulation has been improved in its representations of the geometry of the experiment (plasma gun and flux conserver), the magnetic bias coils, and the detailed time dependence of the current source driving the plasma gun, and uses realistic parameters. The simulations are providing a better understanding of the dominant physics in SSPX, including when the flux surfaces close and the mechanisms limiting the efficiency of electrostatic drive.

PACS: 52.55Ip, 52.65.Kj

## INTRODUCTION

Electron temperatures near 400 eV were observed transiently in the Los Alamos CTX spheromak experiment,<sup>1</sup> and temperatures of 100-200 eV have been observed in the SSPX spheromak.<sup>2</sup> Understanding the energy confinement in these experiments is a challenging problem. Results from numerical simulations with the NIMROD nonlinear resistive MHD code (at zero or finite plasma pressure) have shown that closed flux surfaces with net current can arise only after electrostatic drive is reduced.<sup>3,4</sup> Computations in the last year have directly investigated the importance of inductive effects on energy confinement including the evolution of the temperature and number density using thermal transport coefficients, electrical resistivity, and Ohmic heating. The simulation model is a reasonable approximation because the collisional mean-free path is less than the flux-conserver radius  $R=0.5\text{m}$  for nominal SSPX plasma parameters with  $n\sim 5\times 10^{19}\text{ m}^{-3}$ ,  $T\sim 35\text{ eV}$ , and singly charged ions.

The simulations are performed with the NIMROD code. The simulations solve nonlinear time-dependent equations for particle number density ( $n_i=n_e=n$  with quasineutrality), plasma flow velocity ( $\mathbf{V}$ ), temperature (assuming  $T_i=T_e=T$ ), and magnetic field ( $\mathbf{B}$ ). In MKS units, the evolution equations are

$$\frac{\partial n}{\partial t} + \nabla \cdot (n\mathbf{V}) = \nabla \cdot D \nabla n \quad (1)$$

$$\frac{\partial \mathbf{V}}{\partial t} + \mathbf{V} \cdot \nabla \mathbf{V} = \mathbf{J} \times \mathbf{B} - \nabla p + \nabla \cdot \boldsymbol{\tau} \quad (2)$$

$$\frac{nk_B}{\gamma - 1} \frac{\partial T}{\partial t} + \mathbf{V} \cdot \nabla T = \frac{p}{2} \nabla \cdot \mathbf{V} + \nabla \cdot nk_B \left[ \frac{1}{2} \hat{\mathbf{b}} \hat{\mathbf{b}} + \frac{1}{2} (\mathbf{I} - \hat{\mathbf{b}} \hat{\mathbf{b}}) \right] \cdot \nabla T + \frac{\mathbf{J}^2}{2} \quad (3)$$

$$\frac{\partial \mathbf{B}}{\partial t} = \nabla \times (\mathbf{V} \times \mathbf{B} - \mathbf{J}) \quad (4)$$

$$\nabla_0 \mathbf{J} = \nabla \nabla \mathbf{B} \quad (5)$$

where  $p \equiv 2nk_B T$  is the sum of electron and ion pressures, and  $\hat{\mathbf{b}} \equiv \mathbf{B}/|\mathbf{B}|$  is the evolving magnetic direction vector field. The simulations consider  $n$ ,  $T$ ,  $\mathbf{V}$ ,  $\mathbf{B}$ , and  $\mathbf{J}$  to be functions of all three spatial dimensions and time; thus magnetic fluctuations and anisotropic heat flow are modeled explicitly. The boundary conditions are  $\mathbf{E} \cdot \hat{\mathbf{n}} = \nabla \mathbf{B} \cdot \hat{\mathbf{n}} = \mathbf{v} \cdot \hat{\mathbf{n}} = T = 0$  on the conducting surfaces. The vacuum magnetic fields from coils are assumed to have soaked through the bounding surfaces. The computational grid has been constructed to conform with the conducting surfaces bounding the domain of the plasma gun and flux conserver. The simulations presented use bicubic finite elements to represent the poloidal variations (here we use 24 elements in the direction normal to the electrodes and 32-48 elements parallel to the electrodes) and six toroidal Fourier modes ( $0 \leq m \leq 5$ ).

The parallel and perpendicular thermal diffusivities are  $\chi_{\parallel} = 387 T^{5/2} \text{ m}^2/\text{s}$  and  $\chi_{\perp} = 0.50 T^{1/2} B^2 \text{ m}^2/\text{s}$  ( $B$  in Tesla) based on electrons and ions, respectively, for a hydrogen plasma at  $n = 5 \times 10^{19} \text{ m}^{-3}$ .<sup>5</sup> The numerical computation of  $\chi_{\perp}$  is simplified by using the toroidal average (indicated by  $\langle \rangle$ , hereafter) of the evolving temperature and magnetic induction fields. Similarly, the electrical diffusivity is computed as  $\eta/\eta_0 = 411 (1 \text{ eV}/\langle T \rangle)^{3/2} \text{ m}^2/\text{s}$ . (Numerical tests show no significant deviation from results with a 3D computation of resistivity in the conditions of interest.) An isotropic viscosity ( $\eta$ ) of 100-1000  $\text{m}^2/\text{s}$  is used to provide nonlinear numerical stability during the full-power stage of the current drive. With temperatures of approximately 30 eV during this stage, the Lundquist number (computed as  $S = \eta_0 R v_A / \eta$ , where  $R$  is the radius of

SSPX and  $v_A$  is the Alfvén speed) is of order  $10^6$ . This is much larger than values considered in earlier spheromak simulations.<sup>3,4</sup> The diffusion term in Eq. (1) keeps the density relatively smooth in the absence of particle transport and atomic fueling effects that are not present in the MHD model. The artificial diffusivity ( $D$ ) is set to  $2000 \text{ m}^2/\text{s}$  to help keep the computed minimum of the number density field above zero during strong drive when the MHD activity is violent. For the same reason, the diffusivity is increased locally in computational cells where  $n$  falls to 3% of its volume-averaged value. Because the radiation power is small in most SSPX shots after proper wall conditioning, radiation is not modeled in the NIMROD simulations.

In conditions with sustained coaxial electrostatic drive, the cold edge plasma impedes parallel thermal conduction to the wall, despite the chaotic magnetic topology, allowing the plasma core temperature to reach tens of eVs. When the drive is temporarily removed, relatively symmetric closed flux surfaces form following the resistive decay of symmetry-breaking modes. Magnetic reconnection occurs rapidly in the cold outer plasma, and core temperatures increase toward 100 eV or more. Applying a second current pulse (sustainment pulse), as in some SSPX discharges,<sup>2,6,7</sup> is shown to improve performance by delaying the onset of MHD modes that are resonant in the closed-flux region, and higher current, increased magnetic fields, and larger volumes of closed flux can be achieved. The simulations reveal the sensitivity of the magnetic surfaces and the energy confinement with respect to symmetry-breaking magnetic fluctuations, and the close coupling of the magnetics and the energy transport. We have presented a detailed comparison of nonlinear simulations with laboratory measurements from SSPX<sup>2</sup> and assessed confinement properties of the magnetic configuration in Ref. 8. In this paper,

we present comparisons of NIMROD simulation results to more recent SSPX discharges, and simulations motivated by discharges with repeated injector pulses. The simulation results are yielding electron temperatures, magnetic fields, and fluctuation amplitudes agreeing relatively well with SSPX observations.

The paper is organized as follows. Section II contains a description of simulations directly modeling a series of SSPX shots driven by formation and sustainment pulses. These simulation results agree well with many features in the SSPX data. In this section we also present examples of simulation results and diagnostics highlighting the physics of the magnetic reconnection that accompanies the formation of the spheromak. We describe a few simulations addressing pulsed operation of a spheromak plasma in Section III. We conclude with a brief summary and a discussion of future research directions in Sec. IV.

## **II. SIMULATIONS OF FORMATION AND SUSTAINMENT PULSES IN SSPX**

The SSPX spheromak uses a coaxial plasma gun driven by a capacitor bank to drive current into the expanded region that is the flux conserver.<sup>2,6,7</sup> A set of vacuum magnetic coils provides bias magnetic flux for the spheromak. Figure 1 shows a diagram of the spheromak, the vacuum magnetic field, and the time history of the gun injector current used in the simulations. These were constructed to model a series of shots in SSPX using formation and sustainment pulses. Reference 8 modeled SSPX shots #4620-4642.<sup>2</sup> Here we have retained more of the elongated geometry of the plasma gun and modeled the detailed current-drive history corresponding to shots #10048, 12560 and 12705.

In the NIMROD simulations magnetic flux is driven out of the plasma gun by  $\mathbf{J} \times \mathbf{B}$  forces (Fig. 2) and reconnection occurs (abetted by the action of an MHD instability with toroidal mode  $n=1$  excited by the pinching of the current channel as seen routinely in SSPX in the formation stage and in the CTX<sup>1</sup> and SPHEX<sup>9</sup> experiments). In Figure 3 we show comparisons of the injector current, gun voltage, and poloidal magnetic field measured near the midplane of the flux conserver by an edge probe in NIMROD with measurements from SSPX shot #12705 during formation. Pulsations in the voltage are correlated with oscillations in the poloidal magnetic field history and reconnection events.<sup>10</sup> With detailed field-line tracing using NIMROD simulation data, we are able to see the evolution of the magnetic topology and direct evidence of changes that we interpret as reconnection, e.g., formation of loose knots during formation (Fig. 4). We note that this reconnection is accompanied by the appearance of current sheets with negative values of  $\int \mu_0 \mathbf{J} \cdot \mathbf{B} / B^2$  near the X-point of the toroidally averaged poloidal flux. A detailed examination of reconnection during spheromak formation is presented elsewhere.<sup>10</sup>

In Fig. 5 we compare time histories for the gun current, the poloidal magnetic field measured at an edge probe near the midplane of the flux-conserver, and peak electron temperatures from NIMROD simulation lam06 and SSPX shot #12560. The NIMROD simulation required nearly  $10^5$  time steps and more than  $2.5 \times 10^4$  processor hours extending over two months. The buildup in the poloidal magnetic field in the simulation tracked the experiment until  $t \sim 0.3$  ms where there was an error in the current-drive model (the spike and downward correction in the gun current), which resulted in an accompanying spike and correction in the gun voltage and a steep decrease in the



magnetic field. During the early part of the formation ( $t < 0.3\text{ms}$ ), the simulation sees the  $n=1$  toroidal mode at relative amplitudes similar to SSPX. The emergence of a current-driven  $n=1$  mode during the formation of the spheromak with strong electrostatic drive is typical in both NIMROD simulations and experiments.<sup>1-4,9</sup> After 0.5ms the fluctuations begin to relax in the simulations and in the SSPX shot. At around 4ms  $n=2$  fluctuations emerge in both the simulation and the experiment as the spheromak plasma dies. Figure 6 shows similar fluctuation data from SSPX discharge shot #10048 and lam06. Figure 5 also shows the time history of the peak electron temperature in lam06 and as measured by Thomson scattering in SSPX shot #12560. We note that in this NIMROD simulation we have used a single fluid model with  $T_e=T_i$  assumed. If the ions were in fact colder than the electrons, this would imply that the electron temperature might have to be higher to give the same total pressure as calculated in NIMROD. For the 120eV peak electron temperature, the peak electron  $\beta_e \sim 4\%$  in the simulation.

Figure 7 shows the poloidal magnetic topology (magnetic field-line puncture plot), the corresponding electron temperature contours, and the spatial profile of the SSPX electron temperature from shot #12560. The temperature contours align with the magnetic field as a consequence of the parallel thermal conductivity being orders of magnitude larger than the perpendicular thermal conductivity. Magnetic islands link the temperatures from one side of an island to the other and locally flatten the temperature profile. Closed nested magnetic surfaces are surrounded by confined magnetic field lines that are chaotic, and the field lines are open surrounding the confined region. The transition from chaotic confined field lines to open field lines is accompanied by a steep drop in the electron temperature which tracks the experimental Thomson scattering data

well. Good energy confinement depends strongly on the presence of magnetic surfaces and the quality of the field lines. Electron temperatures of order tens of eV observed on the relatively short open magnetic field lines in the NIMROD simulations are in keeping with calculations in which Ohmic heating balances classical parallel energy transport.<sup>11,12</sup>

The MHD fluctuations tend to correlate with the presence of mode rational surfaces, and Taylor relaxation theory<sup>13</sup> concludes that minimum energy states have flat  $\bar{\psi}$  profiles. Thus,  $\bar{\psi}$  gradients are a source of free energy to drive instability. Figure 8 shows plots of  $\bar{\psi}$  and local safety factor  $q$  at four times as functions of the poloidal flux  $\langle \psi \rangle$ , where  $q = d\langle \psi \rangle / d\langle \phi \rangle$ , and  $\langle \psi \rangle$  and  $\langle \phi \rangle$  are toroidal and poloidal magnetic flux functions of  $\langle \mathbf{B} \rangle$ , respectively. In the region where the toroidally averaged poloidal magnetic flux is closed, we note that the  $\bar{\psi}$  profile is relatively flat and approaches the eigenvalue  $\bar{\psi}_0=9.6$  near the magnetic axis until late in time when a significant  $\bar{\psi}$  gradient emerges accompanying the growth of an  $n=2$  instability that is observed. We also note that the  $q$  profile crosses from above 1/2 to below going from  $t=0.98$ ms to 2ms. Mode rational surfaces, such as  $q=2/3$  and  $q=1/2$ , evidently affect the MHD activity. Observations in SSPX and other NIMROD simulations show correlations between the  $q$  profile crossing low-order mode rational surfaces and the emergence of fluctuations and islands.<sup>6,7,8</sup> Magnetic islands with  $m=2$  are visible in the lam06 simulation at  $t=0.98$ ms after the  $q$  profile has crossed from above 2/3 to below, inside the separatrix. Similarly, an  $m=1$  island appears later in time after the  $q$  profile has crossed  $q=1/2$  inside the separatrix; and the  $m=1, n=2$  mode ultimately grows to significant amplitude (Fig. 6).

### III. SIMULATION OF PULSED SPHEROMAKS

Spheromaks driven by coaxial plasma guns exhibit good confinement transiently. A strong formation pulse followed by a weaker sustaining pulse and decay allow magnetic fluctuations to relax and flux surfaces to emerge, with the highest temperatures appearing during sustainment and decay in experiments.<sup>1,2</sup> The transient formation and decay behavior of spheromak plasmas is supported by simulations.<sup>3,4,8</sup> With coaxial electrostatic current drive, symmetry-breaking fluctuations are needed to introduce a dynamo and provide helicity to maintain the spheromak against resistive decay.<sup>3,4,8</sup> At the same time magnetic fluctuations can spoil the magnetic confinement, and previous simulations have shown that steady electrostatic drive leads to fluctuations that produce chaotic open field lines.<sup>3,4,8</sup> If *steady* coaxial electrostatic current drive does not lead to good magnetic flux surfaces, can cyclically pulsed coaxial electrostatic current drive build high magnetic fields in a spheromak and produce good magnetic surfaces at least transiently in each cycle? We have begun to use NIMROD simulations to address whether pulsed electrostatic drive can be optimized to achieve good energy confinement in a spheromak.

In Figure 9 we display experimental results from SSPX shot #10233 in which there were two injected gun-current pulses.<sup>6</sup> The second pulse in the experiment was able to build the magnetic fields to slightly higher levels in this example. We note that other SSPX shots have achieved significantly higher magnetic fields on the second pulse.<sup>6</sup> The electron temperature response in time shows that local maxima occur during partial decay periods following each of the drive pulses. The NIMROD simulation (sphp09np) shown for comparison agrees qualitatively with SSPX in that the history of the peak temperature

in the simulation shows local maxima in the two decay periods like the experiment and the values of the electron temperature and the poloidal magnetic field in the simulation are similar to those in SSPX. This simulation did not attempt to mimic the experimental pulse shapes for the current drive (the pulse shapes in the simulation were simple 300 kA square pulses, while the pulses in SSPX carried more peak current and were tapered in time); and the magnetic field in the simulation on the second pulse did not grow to a higher value than in the first drive pulse. However, the electron temperature in the second decay period in the simulation achieves a higher value than after the first pulse. The magnetic fluctuation amplitudes are higher during the strong drive periods and relax in the decay periods, during which time closed magnetic flux emerges near the magnetic axis surrounded by chaotic confined field lines (Fig. 10). The larger volume of closed, nested flux surfaces in the lam06 simulation shown earlier with tailored formation and sustainment pulses are accompanied by 50% higher peak injector currents than in sphp09np; the poloidal magnetic fields achieved are ~25% larger; and the peak electron temperatures are twice as large as those shown in Figs. 9 and 10. In both lam06 and sphp09np, the perpendicular thermal conductivity was  $\kappa_{\perp}=21\text{m}^2/\text{s}$ ; and we obtained results very similar to those in sphp09np when we used  $\kappa_{\perp}=15\text{m}^2/\text{s}$  (the minimum values observed in SSPX<sup>2</sup> are  $\kappa_{\perp}=10\text{-}20\text{m}^2/\text{s}$ ).

In Fig. 11 we present the results of simulation sphp09p in which  $\kappa_{\perp}=15\text{m}^2/\text{s}$  and a single 300kA current-drive pulse of twice the duration (~1.2ms) as in sphp09np was used. The edge poloidal magnetic field shows evidence of saturation, and we note that the  $L/R$  time for  $T_e \sim 20\text{-}35\text{eV}$  on open field lines is  $\tau_{L/R} \sim 1\text{ms}$  where the resistivity is  $\eta \sim 10^{-5}\text{Ohm}\cdot\text{m}$  here. The volume of closed, nested magnetic flux is slightly bigger in

the single-pulse simulation than in the double-pulse simulation, and the peak electron temperature achieved during the decay is slightly higher. Overall the differences between the single and double-pulse simulations are small in terms of the spheromak plasmas obtained. The quality of the magnetic confinement is not very good in sphp09np and sphp09p, and these plasmas are significantly colder than in the lam06 simulation. The shaped formation and sustainment pulses in the latter simulations carefully model current-drive pulses used to obtain higher temperature discharges in SSPX. The sustainment pulses and the magnetic flux produced by the bias coils in SSPX and in lam06 and Ref. 8 are constructed to provide a value of  $\bar{\psi}_{gun} \equiv \bar{\psi}_0 I_{gun} / \bar{\psi}_{gun}$ , where  $I_{gun}$  is the gun injector current and  $\bar{\psi}_{gun}$  is the bias magnetic flux at the gun throat, which approximately matches the  $\bar{\psi} = \bar{\psi}_0 \approx 9.6 \text{m}^{-1}$  eigenvalue in the flux conserver. With  $I_{gun} \sim 200 \text{kA}$  ( $\bar{\psi}_{gun} \sim 8.4 \text{m}^{-1}$ ) in the sustainment pulses following formation pulses with higher current, 100-200eV temperature plasmas have been obtained in SSPX and NIMROD simulations. The  $\bar{\psi}_{gun} \sim 12.6 \text{m}^{-1}$  used during the pulsed drive in the sphp09np and sphp09p simulations corresponds to overdriving the spheromak. Overdriving with  $\bar{\psi}_{gun}$  significantly greater than  $\bar{\psi}_0$  has not led to higher temperature shots in SSPX. Experience in SSPX supported by NIMROD simulations suggests that matching  $\bar{\psi}_{gun}$  and  $\bar{\psi}_0$  during sustainment pulses reduces gradients in  $\bar{\psi}$  that drive magnetic fluctuations, and reduced magnetic fluctuations lead to better flux surfaces and higher  $T_e$ .

#### IV. CONCLUSION AND FUTURE DIRECTIONS

The simulations presented here extend those in Ref. 8 in further elucidating the physics affecting spheromak formation and energy confinement, and showing improved agreement between NIMROD simulations and SSPX spheromak observations. The

simulation results support experimental observations in demonstrating that the relaxation of magnetic fluctuations after the spheromak is formed is key to obtaining better energy confinement and high temperatures, but leaves open the question of resupplying the helicity and energy to the spheromak core. The formation of magnetic islands as a consequence of finite-amplitude magnetic fluctuations and the influence of the islands on energy transport are shown in the simulations. The quality of the magnetic field lines is critical to obtaining good energy confinement.

The simulations of pulsed operation of a spheromak are a work in progress. The contrast in the poorer magnetic surfaces and lower temperatures obtained in the pulsed simulations compared to those in the simulations with carefully tailored formation and sustainment pulses that try to match the current pulses used in SSPX indicates the importance of the detailed current-drive time history and the principle derived from SSPX experience that matching  $\bar{I}_{\text{gun}}$  to the  $\bar{I}_0$  eigenvalue in the flux conserver leads to improved energy confinement in the spheromak. Future simulation work will include incorporating the beneficial effects of the sustainment pulses with  $\bar{I}_{\text{gun}} \sim \bar{I}_0$  in controlling the  $q$  profiles and reducing magnetic fluctuations in cyclically pulsed spheromak operation. Future simulations will also address the use of a conducting insert along the geometric axis to help control magnetic fluctuations<sup>14</sup> and additional physics improvements to the simulation model.

We thank T. Kopriva for computing the magnetic field-line trajectories and producing the visualization of the field lines in Fig. 4. We are grateful to L.D. Pearlstein, T.K. Fowler, L.L. LoDestro, members of the SSPX experimental team at Livermore, and the NIMROD team for support, helpful discussions, and encouragement. The simulations

made use of resources at the National Energy Research Supercomputer Center under Department of Energy Contract No. DE-AC03-76SF00098. This work was performed under the auspices of the U.S. Department of Energy under contracts W7405-ENG-48 at the University of California Lawrence Livermore National Laboratory and grant FG02-01ER54661 at the University of Wisconsin-Madison.

## References

1. T. R. Jarboe, *Plasma Phys. Control. Fusion* 36, 945 (1994); T. R. Jarboe *et al.*, *Phys. Rev. Lett.* **51**, 39 (1983).
2. H. S. McLean, *et al.*, *Phys. Rev. Lett.* 88, 125004 (2002); H.S. McLean, S. Woodruff, D.N. Hill, *et al.*, LLNL Laboratory Report UCRL-JC-152827, 30th EPS Conference on Controlled Fusion and Plasma Physics, Saint Petersburg, Russia, July 7-11 2003. *Europhysics conference abstracts*, 27A, p3 230, [http://epsppd.epfl.ch/StPetersburg/PDF/P3\\_230.PDF](http://epsppd.epfl.ch/StPetersburg/PDF/P3_230.PDF)
3. C. R. Sovinec, J. M. Finn, D. del-Castillo-Negrete, *Phys. Plasmas* 8, 475 (2001).
4. R.H. Cohen, H.L. Berk, B.I. Cohen, T.K. Fowler, A.H. Glasser, E.B. Hooper, L.L. LoDestro, E.C. Morse, L.D. Pearlstein, T.D. Rognlien, D.D. Ryutov, C.R. Sovinec, and S. Woodruff, *Nucl. Fusion* **43**, 1220 (2003).
5. S. I. Braginskii, *Reviews of Plasma Physics*, edited by M. A. Leontovich, Vol. 1, p. 205 (Consultants Bureau, New York, 1965).
6. S. Woodruff, B. W. Stallard, H. S. McLean, E. B. Hooper, R. Bulmer, B. I. Cohen, D. N. Hill, C.T. Holcomb, J. Moller, R. D. Wood, "Increasing the magnetic helicity content of a plasma by pulsing a magnetized source," accepted by *Phys. Rev. Lett.*; S. Woodruff, B.I. Cohen, E.B. Hooper, H.S. McLean, B.W. Stallard, D.N. Hill, C.T. Holcomb, C.Romero-Talamas, R.D. Wood, G. Cone, C.R. Sovinec, "Controlled and Spontaneous Magnetic Field Generation in a Gun-Driven Spheromak," submitted to *Phys. Plasmas* (PoP 28362).
7. S. Woodruff, D. N. Hill, E. B. Hooper, J. Moller, H. S. McLean, B. W. Stallard, R. D. Wood, R. Bulmer, B. Cohen, *Phys. Rev. Lett.* **90**, 95001(2003).



8. C.R. Sovinec, B.I. Cohen, G.A. Cone, E.B. Hooper, and H.S. McLean, "Numerical Investigation of Transients in the SSPX Spheromak," submitted to Phys. Rev. Letters (October, 2004).
9. A. al-Karkhy *et al.*, Phys. Rev. Lett. **70**, 1814 (1993).
10. E.B. Hooper, T.A. Kopriva, B. I. Cohen, D.N. Hill, H.S. McLean, R.D. Wood, S. Woodruff, and C.R. Sovinec, "A Magnetic Reconnection Event in a Driven Spheromak," submitted to Phys. Plasmas (November, 2004).
11. E. B. Hooper, R. H. Cohen, and D. D. Ryutov, J. Nucl. Mat. **278**, 104 (2000).
12. R. W. Moses, R. A. Gerwin, and K. F. Schoenberg, Phys. Plasmas **8**, 4839 (2001).
13. J. B. Taylor, Phys. Rev. Lett. **33**, 1139 (1974).
14. D.D. Ryutov, R.H. Cohen, L.D. Pearlstein. Phys. Plasmas **11**, 4740 (2004).

## Figure Captions

Figure 1. (a) Vacuum magnetic fields and spheromak configuration. (b) Injector current time history.

Figure 2. Snapshots of the toroidally averaged poloidal magnetic flux showing spheromak formation in NIMROD simulation lam06.

Figure 3. Injector current, gun voltage, and poloidal magnetic field measured at the midplane of the flux conserver by an edge probe in NIMROD simulation lam07 and measurements from SSPX shot #12705 during formation. Oscillations in the lam07 magnetic energy history correlate with oscillations in the voltage and  $B_z(t)$ .

Figure 4. Toroidally averaged poloidal flux, magnetic field lines, and  $\nabla \cdot \mu_0 \mathbf{J} \cdot \mathbf{B} / B^2$  contours showing topology change in the magnetic field attributed to reconnection. Reconnection is generated by current sheets with negative  $\nabla \cdot \mu_0 \mathbf{J} \cdot \mathbf{B} / B^2$ , which are strongest near the X-point of the mean-field spheromak.

Figure 5. Time histories of the edge poloidal magnetic field at the midplane of the flux conserver, the injector current, and the peak electron temperature in NIMROD simulation lam06 and SSPX shot #12560.

Figure 6. Time histories of the edge-probe poloidal magnetic field fluctuation data from SSPX discharge shot #10048 and simulation lam06.

Figure 7. Magnetic field-line puncture plot at a reference toroidal angle and the corresponding electron temperature contours from simulation lam06, and the spatial profile of the electron temperature from SSPX shot #12560.

Figure 8. Safety factor  $q$  and  $\nabla \cdot \mu_0 \mathbf{J} \cdot \mathbf{B} / B^2$  at four times as functions of the poloidal flux  $\langle \psi \rangle$  in NIMROD simulation lam06.

Figure 9. (a) Time history data from SSPX shot #10233 and (b) time histories of the edge poloidal magnetic field near the midplane of the flux conserver and the peak electron temperature in the NIMROD two-pulse simulation sphp09np.

Figure 10. Magnetic energy time history decomposed by toroidal Fourier mode, and at  $t=2\text{ms}$ :  $\square$  contours, electron temperature contours, and magnetic field-line puncture plot at a reference toroidal angle from the NIMROD two-pulse simulation sphp09np.

Figure 11. Edge poloidal magnetic field time history near the midplane of the flux conserver, temperature time histories in single and double-pulse NIMROD simulations, electron temperature contours and magnetic field-line puncture plot at  $t=1.35\text{ms}$  in the single-pulse simulation sphp09p.

Figure 1

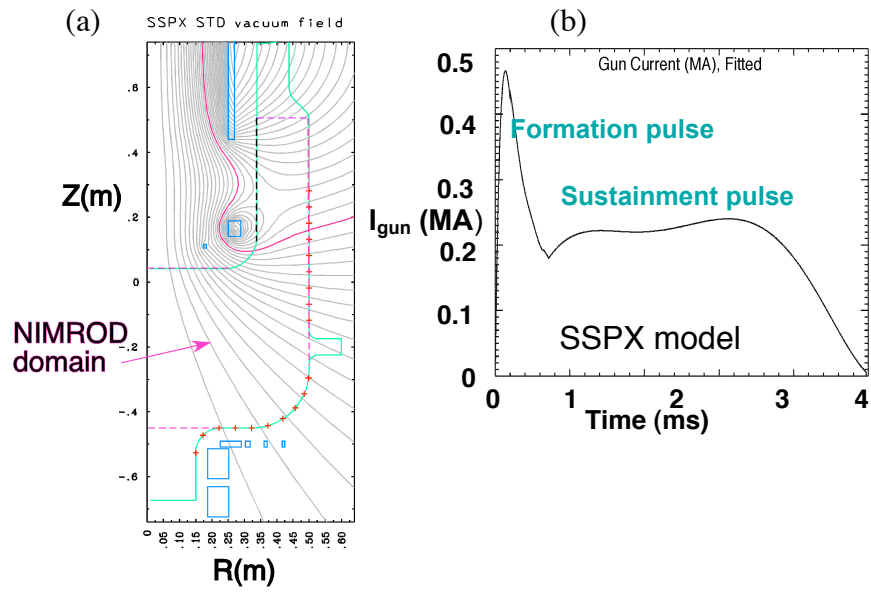


Figure 2

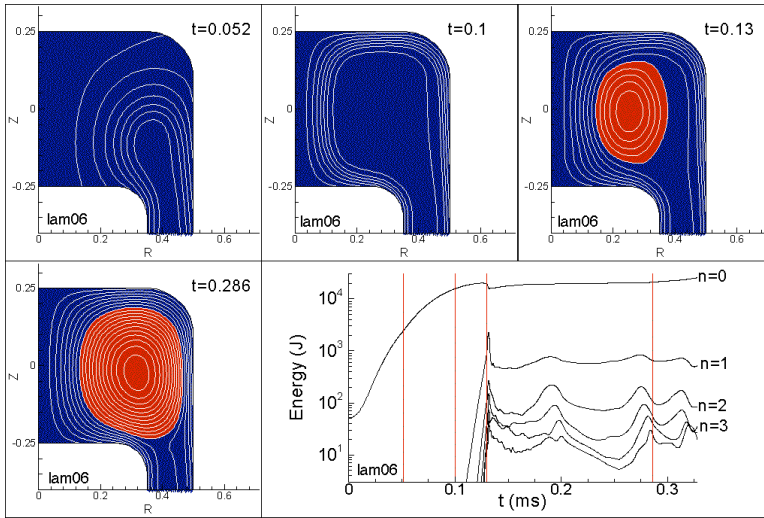


Figure 3

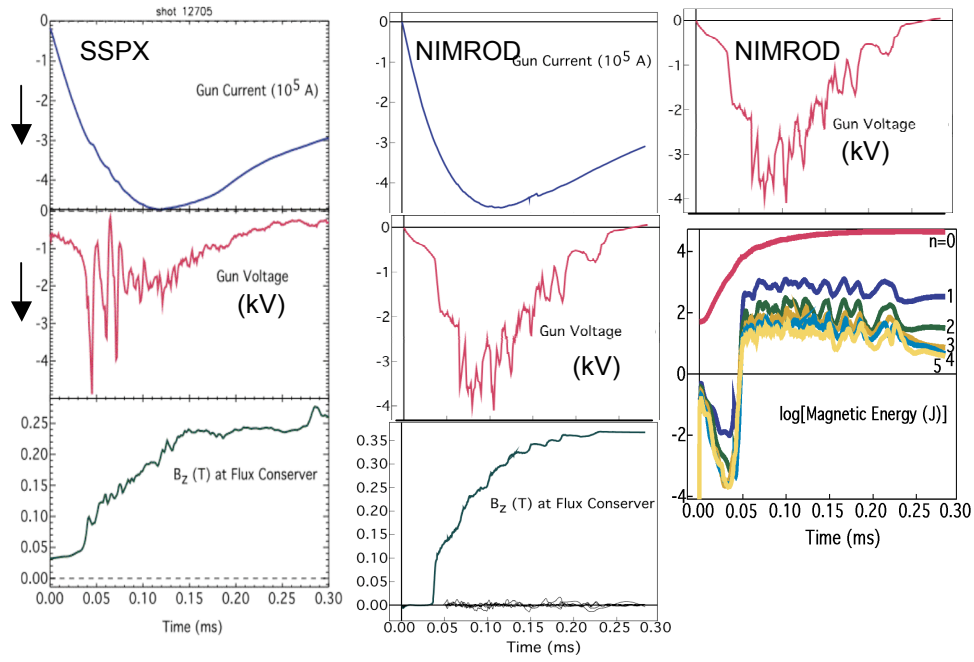


Figure 4

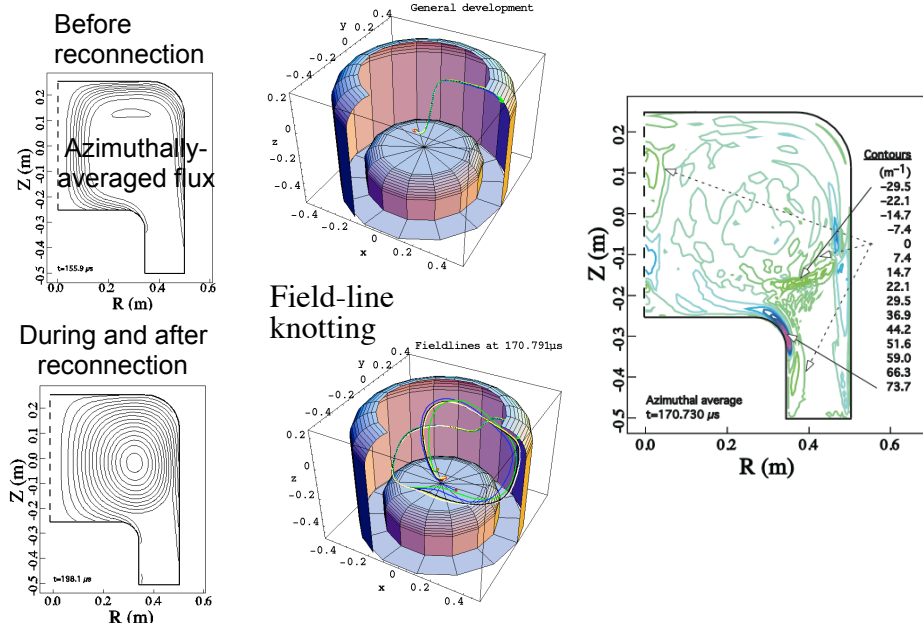


Figure 5

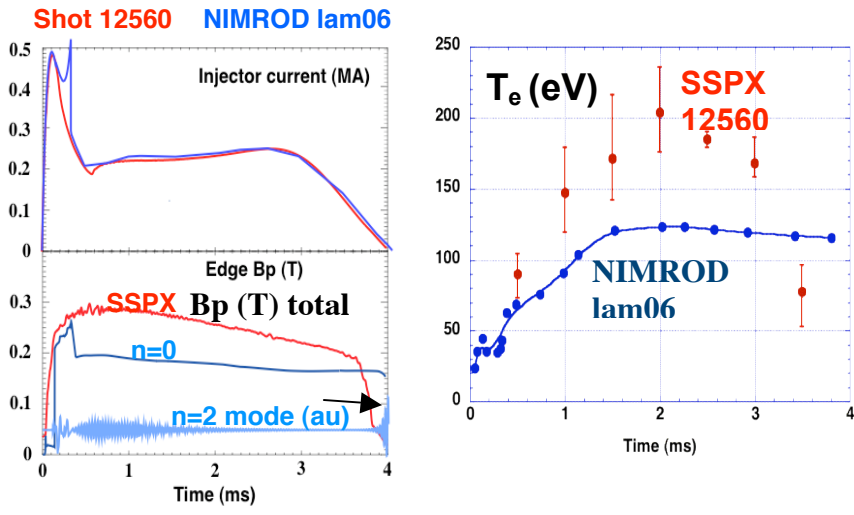




Figure 6

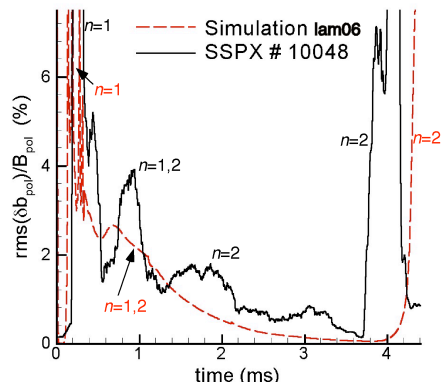


Figure 7

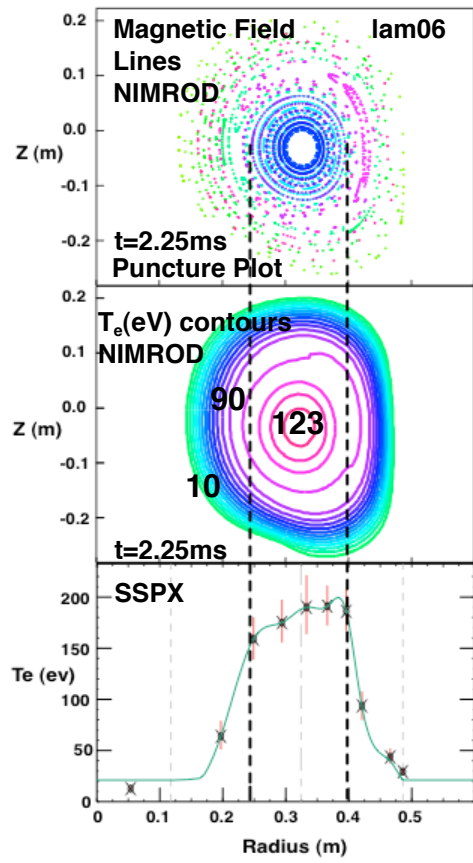


Figure 8

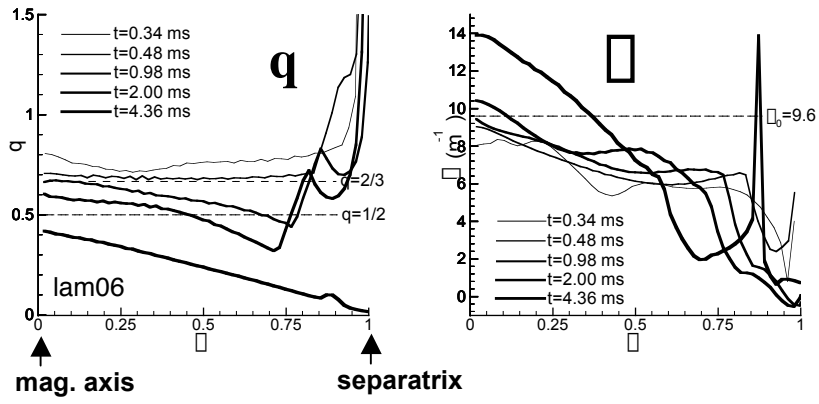


Figure 9

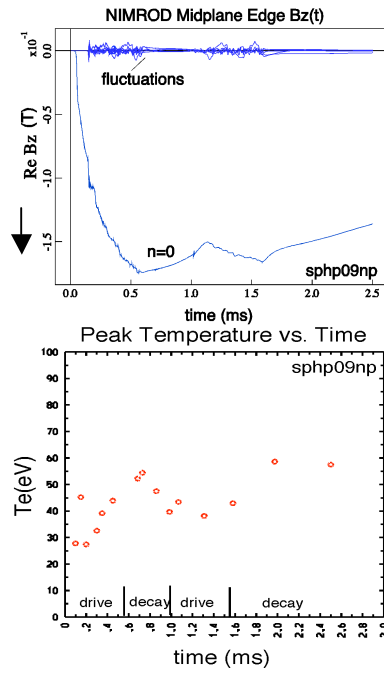
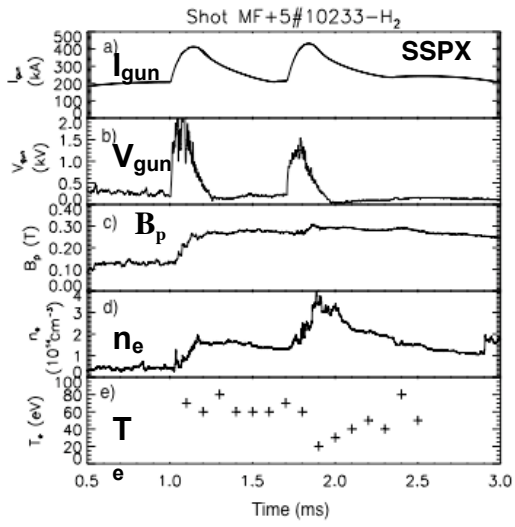


Figure 10

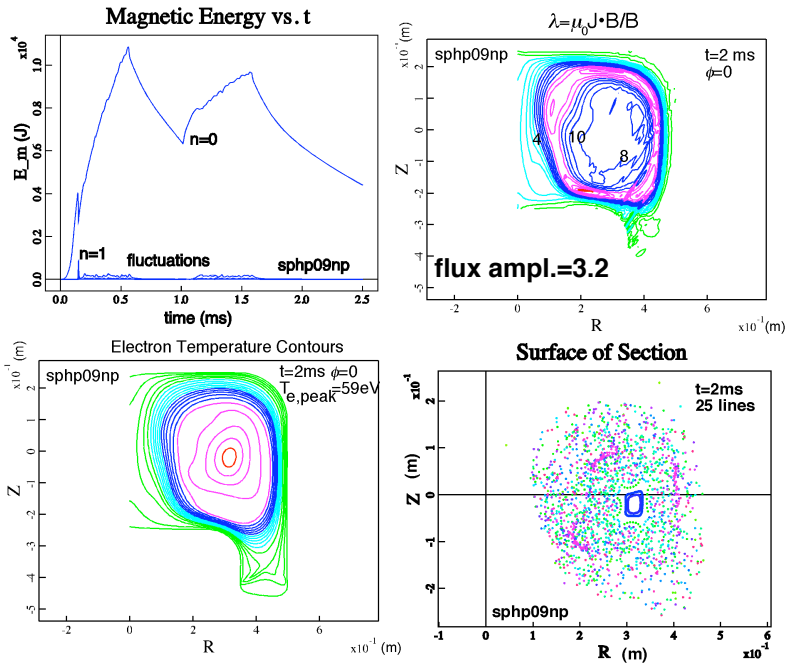


Figure 11

